3D carbon framework-supported CoNi nanoparticles as bifunctional oxygen electrocatalyst for rechargeable Zn-air batteries

Wenjun Wan, Xijun Liu*, Huaiyu Li, Xianyun Peng, Desheng Xi, Jun Luo*

Center for Electron Microscopy and Tianjin Key Lab of Advanced Functional Porous Materials, Institute for New Energy Materials and Low-Carbon Technologies, School of Materials Science and Engineering, Tianjin University of Technology, Tianjin 300384, China

A B S T R A C T

The rational design of optimal bifunctional oxygen electrocatalysts with low cost and high activity is greatly desired for the large-scale implementation of rechargeable Zn-air batteries. Herein, a novel bifunctional electrocatalyst with CoNi alloy nanoparticles supported by a butterfly wing-derived carbon framework (denoted as CoNi/BCF) was synthesized via a pyrolysis method. The obtained CoNi/BCF exhibited excellent oxygen electrocatalytic activity and stability in terms of a positive halfwave potential (0.80 V) for the oxygen reduction reaction (ORR) and a low overpotential (370 mV at 10 mA cm^{-2}) for the oxygen evolution reaction (OER). Remarkably, the high bifunctional ORR/OER activity ($\Delta E_{(ORR-OER)}$ = 0.80 V) also endows an excellent Zn-air battery performance with a high energy density of 853.1 mWh g$_{Zn}^{-1}$, a peak power density of 155.1 mW cm^{-2}, and an excellent cyclability of over 180 cycles at 10 mA cm^{-2}. The satisfactory electrocatalytic performance is due to the synergetic effect between CoNi alloy nanoparticles and nitrogen-doped carbon framework, which includes the high conductivity, highly dispersed active sites and optimized electronic configuration and reaction pathways. Additionally, the smart structures of butterfly wings endow the hybrid catalyst with a large surface area, which is beneficial for the mass transfer, active sites exposure and the fixation of alloy nanoparticles. Our work presents a strategy to take full advantage of natural organisms, rich elements, and naturally optimized smart structures combined in a two-in-one solution, leading to significant improvements in the electrochemical performance. The realization of rechargeable Zn-air batteries also paves a new way for the design and development of efficient and stable electrocatalysts for energy conversion and storage devices.

1. Introduction

Ever-increasing environmental pollution and energy shortage inspire the development of alternative energy storage and conversion systems with high energy densities. Recently, rechargeable Zn-air batteries (ZABs) have attracted extensive attention due to their remarkable high theoretical energy output (1086 Wh kg$_{Zn}^{-1}$), resource abundance, and eco-friendliness [1–6]. Electrocatalysts for oxygen-reduction and oxygen-evolution reactions (ORR and OER, respectively) are crucial for ZABs, where more costly Pt- and Ir/Ru-based materials present the benchmark catalysts for ORR and OER, respectively [7–12]. However, for an industrial use of Zn-air batteries, it is urgently imperative to develop less expensive catalysts, such as cost-effective and robust bifunctional oxygen catalysts based on transition metal elements.

To date, various bifunctional catalysts show promising activity in ORR/OER, including earth-abundant transition metals [13–16], metal-free heteroatom-doped carbon [10,17–20], and metal-nitrogen-doped

carbon [21–24]. Among these catalysts, N-doped carbon materials (such as carbon nanotubes, graphene, and nanocarbon) are attracting great attention for bifunctional electrolysis and ZABs due to their high activity, excellent flexibility, low costs, and versatile design [9,25,26]. The efficient performance can be attributed to the insertion of the N dopants, which leads to changes in the charge and spin distribution of adjacent C atoms due to the higher electronegativity of N compared to C [1,27]. Furthermore, the introduction of transition metal nanoparticles has been proven to significantly enhance the catalyst activity and endow carbon catalysts more promising [28–30]. The synergistic interaction between the metal and N-doped carbon matrix can effectively modify the local electronic structure and thereby optimize the intermediate adsorption, leading to a superior activity comparable to that of precious metal catalysts [8,31,32]. Moreover, the transition metal in the hybrid catalyst has been demonstrated to be converted into metal oxide in oxygen evolution and mitigate the anodic polarization on the carbon material, thereby preventing corrosion of the carbon

support [33]. Even though many inspiring works have made great achievements [11,25,34,35], the synergistic integration of transition metal alloy nanoparticles and a biomass-derived carbon framework as a bifunctional oxygen electrode for ZABs is still limited.

Herein, a hybrid electrode consisting of CoNi alloy nanoparticles grown in situ on a butterfly wing-derived carbon framework (namely CoNi/BCF) has been produced to obtain an efficient and stable bifunctional electrocatalyst for rechargeable ZABs. The as-obtained CoNi/BCF exhibited a positive half-wave potential of 0.80 V for ORR and a low overpotential of 370 mV at 10 mA cm^{-2} for OER. Impressively, when it was integrated into a rechargeable ZAB, a high energy density of 853.1 mWh g$_{Zn}^{-1}$ and a peak power density of 155.1 mW cm^{-2} have been achieved. Furthermore, this as-assembled ZAB also displayed an excellent cycling durability of up to 180 cycles. This excellent bifunctional performance is contributed to its unique structural features and the synergistic effect of CoNi alloy and carbon framework. Specifically, the porous structure of the wing skeleton maintains its double active specific surface area (353.4 m^2 g^{-1}) to offer more exposed active sites for the catalytic reaction. Moreover, the presence of micro/mesopores also increases the transport properties of ORR/OER-relevant species, enhancing the electrochemical kinetics. Furthermore, the combination of CoNi alloy nanoparticles and N-doping can effectively modulate the electronic properties and surface polarities, thus improving the activity of the catalyst. [36–40] In addition, the graphitic N atoms are known to maintain an sp^2-hybridized graphitic structure to improve the electrical conductivity of CoNi/BCF by providing delocalized electrons, which is favorable for the electron transfer during the electrolysis.

2. Experimental section

2.1. Synthesis of CoNi/BCF composite

0.7 mM Co(NO$_3$)$_2$·6H$_2$O, 1.4 mM Ni(NO$_3$)$_2$·6H$_2$O, and 0.7 mM urea were dissolved in 40 mL deionized water and stirred about 10 min until a clear solution was obtained. Then, the solution and 0.12 g butterfly wings were added to a 50 mL Teflon-lined stainless steel autoclave, which was heated at 120 °C for 16 h in an electric oven. Subsequently, the butterfly wings were taken out and dried at 60 °C for 12 h. Then, the prepared butterfly wings were placed into a tube furnace and heated at 800 °C for 2 h under Ar atmosphere. This resulted in the formation of a hybrid catalyst, denoted as CoNi/BCF, consisting of an N-doped carbon framework that was derived from butterfly wings and supported by a CoNi alloy. For comparison, control samples, named as Ni/BCF and Co/BCF, were prepared by adding only either Ni(NO$_3$)$_2$·6H$_2$O or Co(NO$_3$)$_2$·6H$_2$O, respectively, under the same conditions.

2.2. Material characterization

X-ray diffraction (XRD) was performed using the instrument Rigaku Ultima IV in the 2θ range from 10 to 80° at a scan rate of 10° min^{-1}. Morphology and the microstructure of the prepared samples were characterized using a field-emission scanning electron microscope (FESEM; Verios 460 L of FEI) and a transmission electron microscope (TEM; Tecnai G2 F20 S-TWIN, FEI), which were both equipped with an energy dispersive X-ray spectroscope (EDS). Nitrogen adsorption-desorption measurements were performed on an Autosorb-iQ-MP Micromeritics analyzer. Pore volumes and sizes were calculated by the Quenched Solid Density Functional Theory (QSDFT) method, and specific surface areas were calculated by the Brunauer-Emmett-Teller (BET) method. Raman spectroscopy measurements were performed with a high-resolution laser confocal microscopy Raman spectrometer (Horiba evolution) with a 532 nm excitation laser. X-ray photoelectron spectroscopy (XPS) was recorded on a Thermo ESCALAB 250Xi spectrometer with a monochromatic Al K$_{\alpha}$ radiation source, and the C 1 s peak (284.8 eV) has been fixed.

2.3. Electrochemical measurements

All electrochemical tests were performed on a CHI instrument (760E) in a standard three-electrode system using a 0.1 M KOH solution as the electrolyte at room temperature (25 °C). Pt foil, reversible hydrogen electrode (RHE), and rotating disk electrode loaded with the catalyst were used as the counter electrode, reference electrode, and working electrode, respectively. For all tests, the electrolyte was saturated with N$_2$ or O$_2$. To prepare the working electrode, 6.0 mg of the samples was dispersed in a solution containing 500 μL deionized water and 500 μL 0.5 wt.% Nafion solution under sonication. Onto the glassy carbon electrode (GCE, active geometric area 0.196 cm^2 for the RDE and 0.247 cm^2 for the RRDE), 20 μL catalyst ink was dropped and dried at room temperature. The catalyst loading on the electrode was 0.6 mg cm^{-2}. As a comparison, commercial Pt/C and IrO$_2$ (20 wt.%) have a loading of 0.1 mg cm^{-2}. The electrochemical activity of the catalyst was studied via linear sweep voltammetry (LSV) with sweep rates of 10 mV s^{-1} at a rotation rate of 1600 rpm. ORR polarization curves were corrected by subtracting the background current measured under N$_2$ atmosphere. Correction of iR was applied to all initial data for further analysis. Electrochemical impedance spectroscopy (EIS) measurements were performed at an open-circuit voltage in the frequency range from 0.1 Hz to 100 KHz with an alternating current voltage amplitude of 5 mV.

The electron transfer number (n) per oxygen molecule in an ORR process is calculated by the Koutecky-Levich (K–L) equation: [13,19,21]

$$j^{-1} = j_K^{-1} + j_L^{-1} = j_K^{-1} + (B\omega^{1/2})^{-1}$$

$$B = 0.2nFC_O(D_o)^{2/3}v^{-1/6}$$

$$j_k = nFkC_O$$

where j is the measured current density; j_K is the kinetic current density; j_L is the diffusion-limiting current; ω is the electrode rotation rate; B is the slope of the K–L plot; n represents the electron transfer number per oxygen molecule. F is the Faraday constant (F = 96,485 C mol^{-1}). C_o is the bulk concentration of O$_2$ (C_o = 1.2 × 10^{-6} mol cm^{-3}). D_o is the diffusion coefficient of O$_2$ in 0.1 M KOH (D_o = 1.9 × 10^{-5} cm^2 s^{-1}). and v is the kinetic viscosity of the electrolyte (v = 0.01 cm^2 s^{-1}). The coefficient 0.2 indicates a constant that corrects the value when the rotation speed is expressed in rpm.

The total electron-transfer number (n) and hydrogen peroxide yield (%H$_2$O$_2$) were determined by the RRDE approach using:

$$n = 4_{j_D}/[j_D + (j_R/N)]$$

$$\%H_2O_2 = 100[(2j_R/N)/(j_D + (j_R/N))]$$

where j_D and j_R are the voltammetric currents at the disk and ring electrode, respectively. N is the RRDE collection efficiency, which was determined to be 0.37.

2.4. Zn-air battery tests

For the full-cell test of the catalysts, the air electrode consisted of the conductive current collector (nickel foam), the catalyst layer, and the gas diffusion layer. First, the catalyst ink was prepared by mixing CoNi/BCF particles, expandable graphite, activated carbon, and PTFE (60 wt.% PTFE emulsion in water) with a mass ratio of 3 : 3 : 3 : 1. Subsequently, the liquid was uniformly spread on a Ni foam with an area of 2 × 2 cm and then dried at 60 °C for 12 h. The mass loading was 2 mg cm^{-2}. The gas diffusion layer was made up of camphor, 10 wt.% acetylene black, 45 wt.% PVDF, and 25 wt.% PTFE. A polished zinc foil and the air electrode were acted as anode and cathode, respectively. A solution containing 6 M KOH and 0.2 M zinc acetate was used as electrolyte.
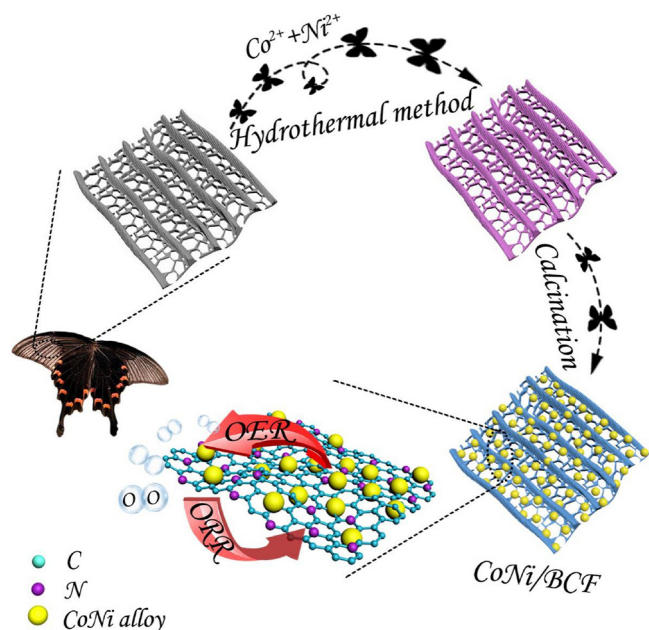
Fig. 1. Schematic illustration of the preparation process of CoNi/BCF electrocatalyst.

3. Results and discussion

3.1. Preparation and structural characterization

The procedure for the synthesis of the hybrid catalyst of CoNi alloy nanoparticles and the N-doped butterfly wing-derived carbon framework and its utilization as a bifunctional electrode for ORR and OER are schematically illustrated in Fig. 1 (see more details in the Experimental Section). The butterfly wings were first immersed in a solution containing cobalt/nickel nitrates to undergo a hydrothermal reaction. Subsequently, cobalt-nickel hydroxyl oxide nanowire arrays were homogeneously generated on the surfaces of the butterfly wings (**Figs. S1** and **S2**). After drying and further carbonization at 800 °C for 2 h under Ar atmosphere, the butterfly wings had been transformed into carbon frameworks, and the cobalt-nickel hydroxyl oxides had been simultaneously decomposed into CoNi alloy nanoparticles. Of note, the hierarchical structure of raw butterfly wings was maintained well. More importantly, in situ nitrogen doping of the carbon frameworks had also been simultaneously achieved through the high-temperature pyrolysis of the butterfly wings due to their nitrogen-rich composition confirmed by our previous work. [39–41] Further characterization will be shown later.

Morphology and structure of the as-prepared materials were investigated by FESEM, TEM, STEM and HRTEM measurements. Fig. 2a, b show the typical SEM images of CoNi/BCF at various magnifications. Apparently, the resulting hybrid has well-retained scales of two or more layers, although the skeleton and internal void of the hybrid shrank markedly after pyrolysis (**Fig. S3**). The hybrid scales clearly show rough surfaces compared with the pristine BCF (**Figs. 2**b, c and **S4**), owing to the decoration with CoNi alloy nanoparticles. As displayed in the inset of Fig. 2c, these nanoparticles were monodispersed and possessed an average size of 38.3 nm. The internal structure of CoNi/BCF elucidated by STEM and TEM further revealed that the nanoparticles were uniformly distributed on the graphene-graphite films (GGFs), which was supported by the porous skeleton of the wing scales (Fig. 2c, d). The lattice fringe of CoNi/BCF with a *d*-spacing of 0.1739 nm (Fig. 2e), which is close to that of Co (0.1772 nm, JCPDS 15-0806) and Ni (0.1762 nm, JCPDS 04-0850), can be assigned to the (200) planes of metallic Co and Ni. And the lattice fringe of 0.2025 nm of CoNi/BCF is

close to the standard lattice fringes of Co (0.2047 nm, JCPDS15-0806) and Ni (0.2034 nm, JCPDS 04-0850), which correspond to the (111) lattice planes of Co and Ni, respectively. [28] Furthermore, we observed a *d*-spacing of 0.33 nm, corresponding to the (002) plane of graphitic carbon (Fig. 2f). Of note, different layers of graphitic shells constitute the GGFs. As previously reported, [39,40] the formation mechanism of the GGFs can be explained by the diffusion and release of carbon through the CoNi alloy nanoparticles. EDS of CoNi/BCF clearly shows a uniform distribution of N throughout the GGFs and further gives an atomic ratio of 1 : 2.7 (Co : Ni) for the CoNi alloy (Fig. 2g). Two control samples (namely Co/BCF and Ni/BCF) were prepared by the same procedure as applied for CoNi/BCF, without using $Ni(NO_3)_2$ or $Co(NO_3)_2$. The SEM images in **Figs. S5** and **S6** demonstrate that both control samples and CoNi/BCF possess very similar morphologies.

The XRD patterns of the as-obtained samples (Fig. 3a) show three diffraction peaks at $2\theta = 44.41°$, $51.75°$, and $76.26°$, which could be fitted to the (111), (200), and (220) planes of metallic Co (JCPDS 15-0806) or Ni (JCPDS 04-0850). The diffraction peak positions of CoNi/BCF are in agreement with those of the stable face-centered cubic phase CoNi nanowires obtained by Mehmood et al. [42,43] Moreover, CoNi/BCF and BCF displayed both two very broad 2θ peaks at 24.46° and 43.62°, characteristic for the disordered structure of the butterfly wing-derived carbon framework (Figs. 3a and S7). In addition, the XRD patterns of Co/BCF and Ni/BCF (**Fig. S7**) confirm the presence of metallic Co and Ni nanoparticles. Furthermore, Raman spectra demonstrate that CoNi/BCF has a smaller I_D/I_G value (refers to the intensity ratio of D band to G band) than that of the control samples (**Fig. S8**), suggesting CoNi/BCF possesses a higher degree of graphitization [9,20]. This speculation is further verified by the XPS analysis (**Fig. S9**). Customarily, a high degree of graphitization is expected to bring out an improved electrical conductivity, which is beneficial for the charge transfer during the electrolysis.

The textural characteristics of the as-synthesized samples were analyzed by BET measurements (**Figs. 3**b, c and **S10**). The specific surface area (SSA) of CoNi/BCF has been measured to be 353.4 m^2 g^{-1}, which is largest than those of Co/BCF (289.1 m^2 g^{-1}), Ni/BCF (343.5 m^2 g^{-1}), and BCF (312.2 m^2 g^{-1}). The type IV hysteresis adsorption plot confirms the micro/mesoporosity of CoNi/BCF. The corresponding pore size distribution (Fig. 3c) was analyzed by the QSDFT model, revealing good agreement with previous reports [36]. CoNi/BCF exhibited clearly some amount of micropores and mesopores, the maximum pore width of around 3.8 nm was measured. A previous study assumed that the active sites were hosted in the micropores [44]. Moreover, the mesoporous structure not only improved the mass transfer but also provided a highly accessible surface area for the electrolysis [45,46].

Chemical composition and bonding configuration of CoNi/BCF were further investigated by XPS. The high-resolution XPS spectrum of Co 2p (Fig. 3d) shows two fitted peaks for Co 2p$_{3/2}$ that can be assigned to Co^{3+} (778.7 eV) and Co^{2+} (781.6 eV), respectively [8,11,47]. Likewise, the peak of Ni 2p$_{3/2}$ (Fig. 3e) can be deconvoluted into two peaks attributed to Ni^{3+} (856.1 eV) and Ni^{2+} (852.8 eV) [28,48,49]. Apparently, both Co 2p and Ni 2p spectra reveal the inevitable oxidation of partial surface atoms in the CoNi alloy. Due to their moderate metallicity, the trace surface oxides are incapable of arousing diffraction in the XRD pattern (Fig. 3a). Moreover, the high-resolution N 1s spectrum (Fig. 3f) can be deconvoluted into four subpeaks located at 398.8 eV (pyridinic-N, 37.2 at.%), 400.6 eV (pyrrolic-N, 30.3 at.%), 401.3 eV (graphitic-N, 25.1 at.%), and 403.4 eV (oxidized-N, 7.4 at.%) [13,25]. Recent studies claimed that pyridinic-N and graphitic-N are helpful in boosting oxygen adsorption and reducing the ORR overpotential through their excellent electron-accepting ability [50–52], while pyridinic-N and pyrrolic-N can serve as metal coordination sites owing to their lone-pair electrons [53].
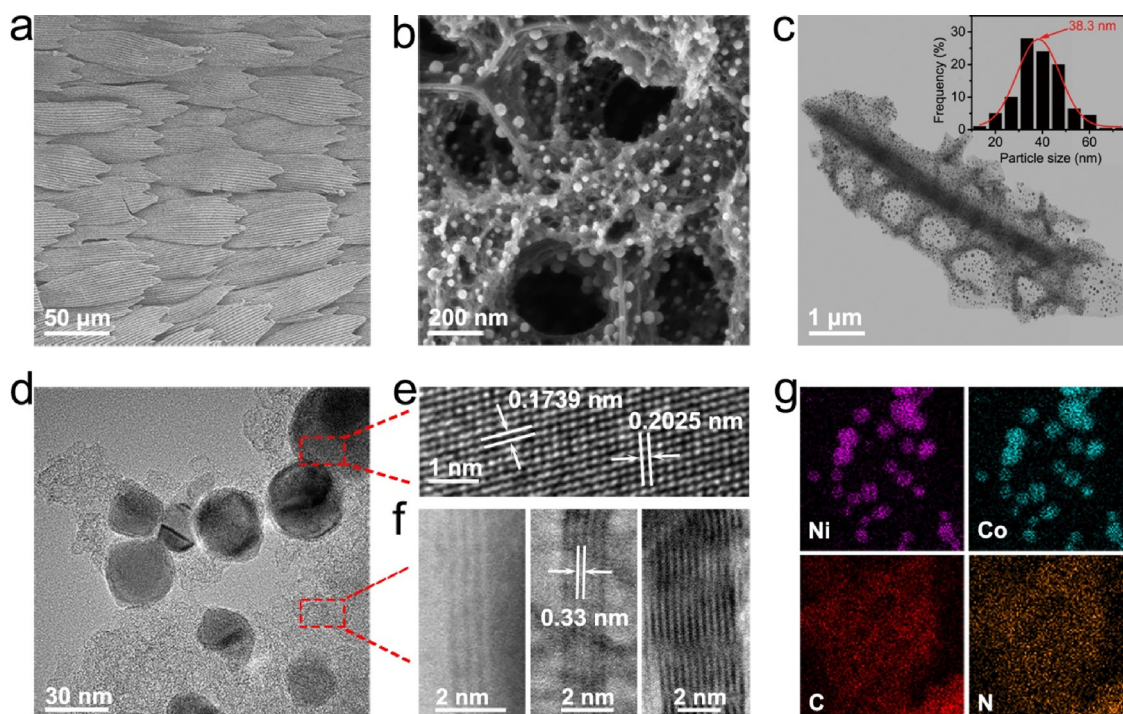
Fig. 2. Morphological and structural characterization of CoNi/BCF. (a, b) High- and low- magnification FESEM images; (c) STEM image, inset in (c) is the size distribution of CoNi alloy nanoparticles; (d) TEM image; (e, f) HRTEM images; (g) EDS mapping of CoNi/BCF.
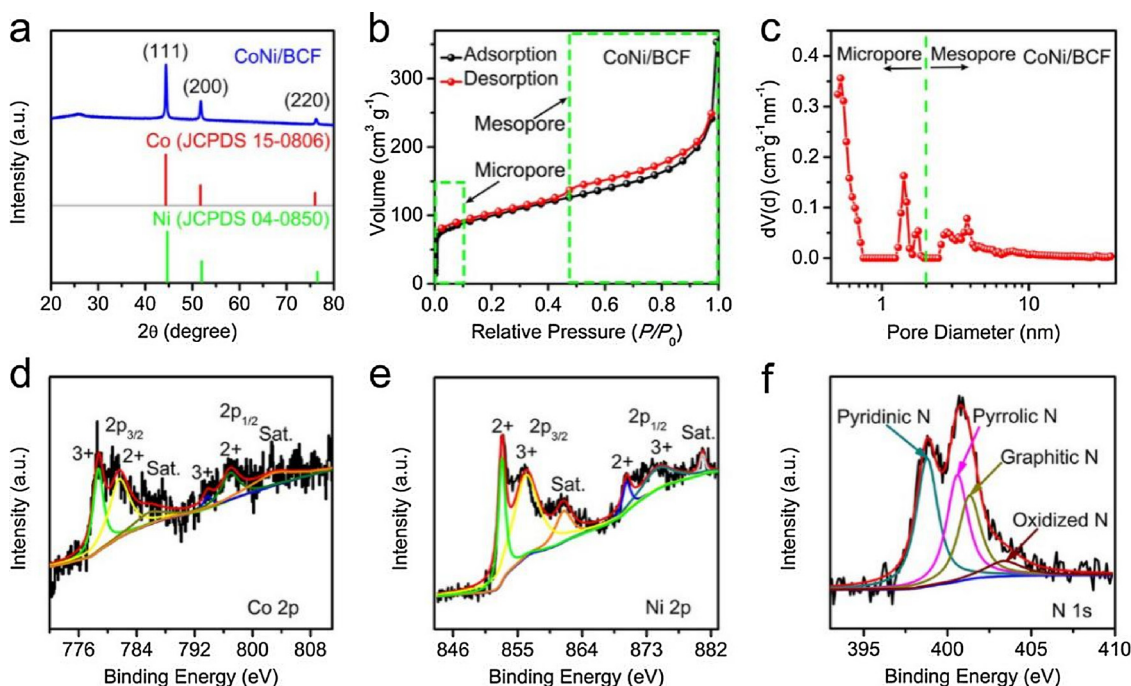

Fig. 3. Composition and textural characterization of CoNi/BCF. (a) XRD patterns; (b, c) Nitrogen adsorption/desorption isotherms and corresponding calculated pore size distribution; (d–f) XPS spectra of Co 2p, Ni 2p and N 1 s.

3.2. Evaluating the electrocatalytic activity of CoNi/BCF

It can be assumed that the micro/mesoporous structure of CoNi/BCF will be not only beneficial for both gas and electrolyte diffusion during the electrolysis but also supply a great number of exposed edge sites. More importantly, the synergistic effects between CoNi alloy nanoparticles and N-doped BCF will contribute to an enhanced electrocatalytic activity for ORR/OER. Therefore, the catalytic performance of CoNi/BCF and control samples for both ORR and OER were evaluated

and compared based on rotating disk electrode (RDE) measurements in O_2-saturated 0.1 M KOH at a sweep rate of 10 mV s^{-1} and a rotation rate of 1600 rpm (see more details in the Experimental Section). The ohmic potential drop losses from the solution resistance were applied to all initial data [51,54,55], and all potential values given for ORR/OER in this work were referenced to the reversible hydrogen electrode (RHE). In **Fig. S11**, a noticeable reduction peak is observed for CoNi/BCF in O_2-saturated solution. The polarization curves reveal a much higher ORR activity for CoNi/BCF than for Co/NCF, Ni/BCF, and BCF.
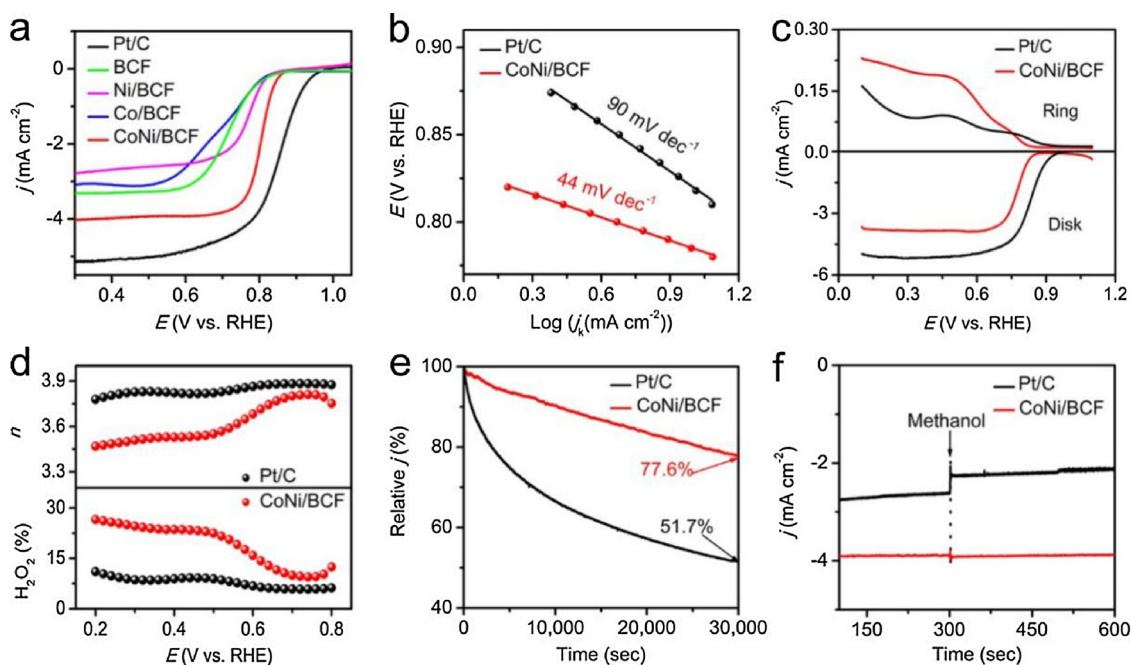
Fig. 4. ORR performance of CoNi/BCF. (a) RDE polarization curves; (b) Corresponding Tafel plots of ORR activity in (a); (c) RRDE results; (d) The H_2O_2 yield and the electron number of transferred calculated from panel (c); (e) Chronoamperometric responses for CoNi/BCF and Pt/C at 0.7 V; (f) Methanol crossover tests by the introduction of 3.0 M methanol into the electrolyte. All experiments were conducted in 0.1 M KOH at ambient temperature and pressure.

Onset potential (E_{onset}) and half-wave potential ($E_{1/2}$) of CoNi/BCF are 0.91 V and 0.80 V (Fig. 4a), respectively, both of which are more positive than those of the control samples (see details in **Table S1**). Although E_{onset} and $E_{1/2}$ for CoNi/BCF are inferior to those of Pt/C, the kinetics of CoNi/BCF is a more favorable compared to those of Pt/C (Fig. 4b). To further clarify the ORR kinetics, rotating ring-disk electrode (RRDE) measurements were performed. As shown in Fig. 4c, d, the average transferred electron number (n) is 3.77, suggesting a four-electron reaction pathway for ORR. Furthermore, the fitted K–L plots of CoNi/BCF reveal a desirable four-electron reaction pathway dominating the ORR process with negligible formation of peroxide intermediates (**Fig. S12**). In addition, the yield of HO_2^- is below 15% at 0.6 – 0.8 V. Moreover, after 30,000 s continuous electrolysis, CoNi/BCF shows a more stable durability than Pt/C (Fig. 4e). The current drop for CoNi/BCF and Pt/C is 22.4 and 48.3%, respectively. Furthermore, a better methanol tolerance is also expected for CoNi/BCF (Fig. 4f).

In addition to the efficient ORR electrocatalytic performance, CoNi/BCF also efficiently catalysed OER. As shown in Fig. 5a, CoNi/BCF delivers an OER current density of 10 mA cm^{-2} with a potential of 1.60 V, namely $E_{j = 10} = 1.60$ V, which is lower than the corresponding potentials of Co/BCF (1.64 V), Ni/BCF (1.64 V), and IrO_2 (1.76 V). This result indicates the excellent OER performance of CoNi/BCF, which is further confirmed by its lower Tafel slope as compared to Pt/C (Fig. 5b). The potential gap ΔE between $E_{j = 10}$ and $E_{1/2}$ is widely used to assess the bifunctional activity of catalysts. [56,57] In principle, a lower value of ΔE indicates a better bifunctional activity. The remarkable ORR and OER bifunctional activity of CoNi/BCF is reflected in the lowest ΔE of 0.80 V (Fig. 5c). This value is also comparable to or lower than that of the most active bifunctional electrocatalysts reported to date (see details in **Table S2**). The above results have shown that CoNi/BCF exhibits superior activity in comparison to the Co/BCF and Ni/BCF counterparts, which is possibly due to the following reasons. Frist, a larger specific surface area of CoNi/BCF offers more accessible active sites (Figs. 3b and **S10**). Second, the increased graphitization of carbon phase in CoNi/BCF endows a better electrical conductivity (**Fig. S8**). Third, the reduced charge transfer resistance of CoNi/BCF contributes faster electron-transfer kinetics (**Fig. S13**). Fourth, the bonding

between the two dissimilar metals (i.e., Co and Ni) can establish intrinsic polarity that induces an electronic modulation and optimized reaction pathways, [28,38] both of which are beneficial to the enhanced electrocatalytic activity.

These promising electrochemical performances of CoNi/BCF catalysts for both ORR and OER can be attributed to following two aspects: (1) the porous structure of the wing skeleton maintains the ample and double-faced exposure of the GGFs, [40] making the uniformly anchored CoNi alloy nanoparticles fully accessible to accelerate the mass transfer; (2) the integration of CoNi alloy nanoparticles with N-doping can modulate the electronic properties and surface polarities [36,58], thus improving the activity of the catalyst.

3.3. Rechargeable zinc–air battery studies of CoNi/BCF

In light of the prominent bifunctional activity of CoNi/BCF, a rechargeable ZAB has been assembled to demonstrate that CoNi/BCF can be applied in real energy-related devices. As illustrated in Fig. 6a, 6 M KOH containing 0.2 M zinc acetate were used as the electrolyte; a Zn plate served as the anode, and CoNi/BCF-loaded nickel foam (~2 mg cm^{-2}) loaded with a gas diffusion layer as the air cathode. For comparison, the Pt/C + IrO_2 couple (Pt/C : IrO_2 mass ratio of 1 : 1) has been tested under the same conditions. The open-circuit voltage of the assembled ZAB is about 1.44 V (Fig. 6b), which is close to that of Pt/C + IrO_2. The charge/discharge polarization curves and the corresponding power density plots are depicted in Fig. 6c. At a voltage of 1.0 V, CoNi/BCF shows a current density of 120.2 mA cm^{-2}, which is higher than that of Pt/C + IrO_2 (84.8 mA cm^{-2}). Significantly, the maximum power density of CoNi/BCF has been determined to be 155.1 mW cm^{-2} (197.6 mA cm^{-2}), which is higher than that of Pt/C + IrO_2 (104.7 mW cm^{-2} at 150.1 mA cm^{-2}). When galvanostatically discharged at 10 mA cm^{-2}, the CoNi/BCF-catalyzed ZAB delivered a stable discharge voltage around 1.2 V without any obvious degradation (Fig. 6d). The specific capacity at 10 mA cm^{-2} has been calculated to be as high as ~ 710.9 mA h g$_{Zn}^{-1}$, normalized to the mass of consumed Zn (corresponding to ~ 86.7% of the theoretical capacity). The corresponding energy density has been estimated to be ~ 853.1 mWh g$_{Zn}^{-1}$.
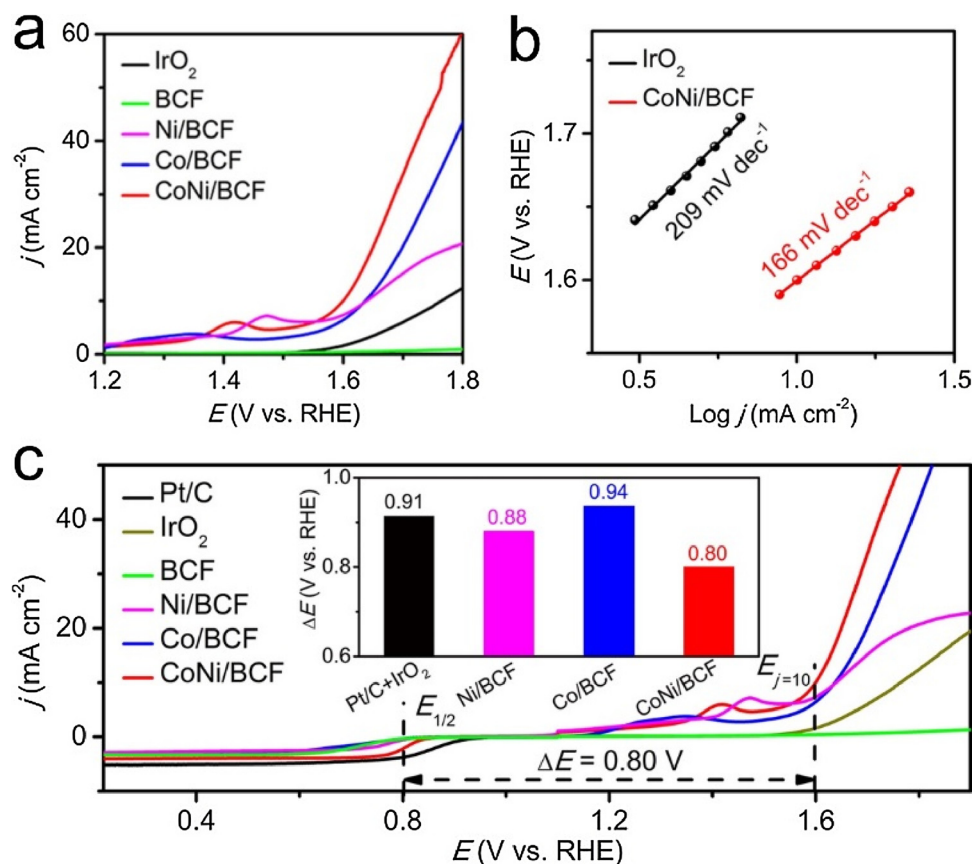
Fig. 5. OER performance of CoNi/BCF. (a) RDE polarization curves; (b) Corresponding Tafel plots of OER activity in (a); (c) Polarization curves of different catalysts for both ORR and OER, the inset is the potential gap (ΔE) between $E_{j\,=\,10}$ and $E_{1/2}$ for all the catalysts. All experiments were conducted in 0.1 M KOH at ambient temperature and pressure.

Furthermore, the cycling stability of the batteries was measured by charge and discharge cycles at 10 mA cm^{-2} (Fig. 6e). Clearly, the CoNi/BCF catalysed ZAB exhibits a good durability with short cycle times (10 min per charge or discharge period). By contrast, the battery based on Pt/C + IrO$_2$ displays a voltage decrease in the discharge process and

a voltage increase in the charge process, probably due to oxidation and loss of precious metals during the charge process [59]. As an impressive exemplification for practical applications, a CoNi/BCF catalysed ZAB can power a timer (Fig. 6f). The above results indicate that CoNi/BCF can enable ZABs with a high efficiency and a long cycle life, even
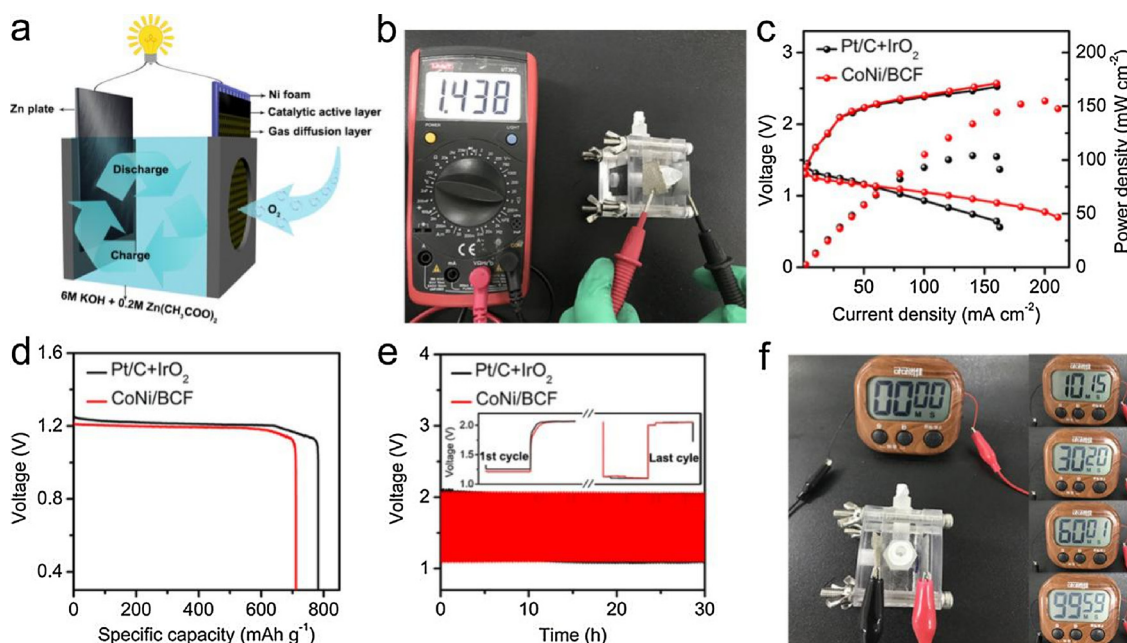

Fig. 6. Electrochemical performance of ZAB using CoNi/BCF. (a) Schematic illustration of a Zn-air battery; (b) Photograph of a ZAB based on CoNi/BCF with an open-circuit voltage of 1.44 V; (c) Charging and discharging polarization curves and corresponding calculated discharge power density; (d) Typical specific capacity curves recorded at 10 mA cm^{-2} discharging rate; (e) Long time cycling test at 10 mA cm^{-2}; (f) Photograph showing a timer running by ZAB using CoNi/BCF as the cathode.

comparable of the recently best reported bifunctional catalysts (see **Table S3** for details). For example, Chen et al. prepared MnO@Co-N/C nanowires [30], which showed a peak power density of 130.3 mW cm^{-2} and a good durability (1900 cycles for 633 h at 5 mA cm^{-2}). Wang et al. reported that anion-regulated NiFe hydroxysulfdes ($Ni_{1.9}FeS_{1.09}(OH)_{4.6}$) grown on Ni foam was able to deliver a high peak power density of 248 mW cm^{-2}, as well as a remarkable cycling stability over 25 h of operation at a current density of 2.0 mA cm^{-2} [37]. Chen et al. designed and fabricated Pd nanoparticles supported on boron carbide (Pd/B_4C) and investigated its performance in ZAB, which could achieve a peak power density of 187 mW cm^{-2} and a cyclic stability (up to 1333 h at 5 mA cm^{-2}) [32]. These are all significant researches for ZABs. A further comparison of the three different air cathodes (i.e., MnO@Co-N/C, $Ni_{1.9}FeS_{1.09}(OH)_{4.6}$, and CoNi/BCF) revealed that transitional metal-based catalysts can be promising alternatives to the costly precious metal-based materials by optimization of catalyst designs. Meanwhile, exploring new and cost-effective approaches to fabricate ZAB air-cathodes is highly useful for the commercialization of electrically ZABs.

4. Conclusions

In conclusion, a novel bifunctional catalyst composed of CoNi alloy nanoparticles and a 3D butterfly wing-derived carbon framework has been successfully developed in this study. The resulting catalyst exhibits an excellent electrocatalytic activity and stability for both OER and ORR in terms of a low overpotential (370 mV at 10 mA cm^{-2}) for OER, a positive half-wave potential (0.80 V) for ORR, and especially, the obtained Zn-air batteries showed an open-circuit potential of 1.44 V, a maximum power density of 155.1 mW cm^{-2}, as well as an excellent cyclability (180 cycles for 60 h). The synergetic effect between NiCo alloy nanoparticles and the N-doped carbon framework was considered as the main contribution for the excellent catalytic activities of the hybrid catalyst, including of high electrical conductivity, highly dispersed active sites and optimized electronic structure and reaction pathways. In addition, the porous skeleton of wing scales ensures the two-dimensional spreading and double-face exposure of the GGFs. These GGFs not only increase the surface area of this hybrid catalyst but also favor the fixation of the alloy nanoparticles on GGFs surface. Undoubtedly, this work will promote the development of transition metal alloy-based hybrid materials for applications in ORR/OER electrocatalysis. Moreover, the usage of butterfly wings with naturally optimized smart structures will provide a new avenue for designing other biomass-derived carbon materials for renewable energy systems.

Acknowledgments

Appendix A. Supplementary data

Supplementary material related to this article can be found, in the online version, at doi:https://doi.org/10.1016/j.apcatb.2018.08.081.

References

[1] D.J. Yang, L.J. Zhang, X.C. Yan, X.D. Yao, Small Methods 1 (2017) 1700209.
[2] Y.G. Li, H.J. Dai, Chem. Soc. Rev. 43 (2014) 5257–5275.
[3] J. Pan, Y.Y. Xu, H. Yang, Z.H. Dong, H.F. Liu, B.Y. Xia, Adv. Sci. 4 (2018) 1700691.
[4] J. Fu, Z.P. Cano, M.G. Park, A.P. Yu, M. Fowler, Z.W. Chen, Adv. Mater. 29 (2017) 1604685.
[5] P. Tan, B. Chen, H.R. Xu, H.C. Zhang, W.Z. Cai, M. Ni, M.L. Liu, Z.P. Shao, Energy Environ. Sci. 10 (2017) 2056–2080.
[6] J. Park, M. Park, G. Nam, J.S. Lee, J. Cho, Adv. Mater. 27 (2015) 1396–1401.
[7] Y.Q. Zhang, M. Li, B. Hua, Y. Wang, Y.F. Sun, J.L. Luo, Appl. Catal. B-Environ. 236 (2018) 413–419.
[8] X.P. Han, X.Y. Wu, C. Zhong, Y.D. Deng, N.Q. Zhao, W.B. Hu, Nano Energy 31 (2017) 541–550.
[9] J. Wang, H.H. Wu, D.F. Gao, S. Miao, G.X. Wang, X.H. Bao, Nano Energy 13 (2015) 387–396.
[10] J.T. Zhang, Z.H. Zhao, Z.H. Xia, L.M. Dai, Nat. Nanotechnol. 10 (2015) 444–452.
[11] H. Cheng, M.L. Li, C.Y. Su, N. Li, Z.Q. Liu, Adv. Funct. Mater. 27 (2017) 1701833.
[12] X.E. Liu, M. Park, M.G. Kim, S. Gupta, X.J. Wang, G. Wu, J. Cho, Nano Energy 20 (2016) 315–325.
[13] F.L. Meng, H.X. Zhong, J.M. Yan, X.B. Zhang, Nano Res. 10 (2017) 4436–4447.
[14] Y.C. Fan, S. Ida, A. Staykov, T. Akbay, H. Hagiwara, J. Matsuda, K. Kaneko, T. Ishihara, Small 13 (2017) 1700099.
[15] A. Zitolo, V. Goellner, V. Armel, M.T. Sougrati, T. Mineva, L. Stievano, E. Fonda, F. Jaouen, Nat. Mater. 14 (2015) 937–944.
[16] Y.Y. Guo, P.F. Yuan, J.N. Zhang, Y.F. Hu, I.S. Amiinu, X. Wang, J.G. Zhou, H.C. Xia, Z.B. Song, Q. Xu, S.C. Mu, ACS Nano 12 (2018) 1894–1901.
[17] M.C. Wu, T.S. Zhao, H.R. Jiang, L. Wei, Z.H. Zhang, Electrochim. Acta 222 (2016) 1438–1444.
[18] G.L. Chai, K.P. Qiu, M. Qiao, M.M. Titirici, C.X. Shang, Z.X. Guo, Energy Environ. Sci. 10 (2017) 1186–1195.
[19] H. Luo, W.J. Jiang, Y. Zhang, S. Niu, T. Tang, L.B. Huang, Y.Y. Chen, Z.B. Wei, J.S. Hu, Carbon 128 (2018) 97–105.
[20] X. Zhang, C.Y. Wang, Y.N. Chen, X.G. Wang, Z.J. Xie, Z. Zhou, J. Power Sources 377 (2018) 136–141.
[21] Y.X. Zhao, Q.X. Lai, Y. Wang, J.J. Zhu, Y.Y. Liang, ACS Appl. Mater. Interfaces 9 (2017) 16178–16186.
[22] H.W. Liang, W. Wei, Z.S. Wu, X.L. Feng, K. Müllen, J. Am. Chem. Soc. 135 (2013) 16002–16005.
[23] U. Tylus, Q.Y. Jia, K. Strickland, N. Ramaswamy, A. Serov, P. Atanassov, S. Mukerjee, J. Phys. Chem. C 118 (2014) 8999–9008.
[24] B.W. Wang, X.X. Wang, J.X. Zou, Y.C. Yan, S.H. Xie, G.Z. Hu, Y.G. Li, A.G. Dong, Nano Lett. 17 (2017) 2003–2009.
[25] R. Nandan, K.K. Nanda, J. Mater. Chem. A Mater. Energy Sustain. 5 (2017) 16843–16853.
[26] T.R. Zhan, X.L. Liu, S.S. Lu, W.G. Hou, Appl. Catal. B- Environ. 205 (2017) 551–558.
[27] Y.C. Hao, Z.Y. Lu, G.X. Zhang, Z. Chang, L. Luo, X.M. Sun, Energy Technol. 5 (2017) 1265–1271.
[28] Y. Fu, H.Y. Yu, C. Jiang, T.H. Zhang, R. Zhan, X.W. Li, J.F. Li, J.H. Tian, R.Z. Yang, Adv. Funct. Mater. 9 (2018) 1705094.
[29] T.H. Zhou, Y.H. Du, S.M. Yin, X.Z. Tian, H.B. Yang, X. Wang, B. Liu, H.M. Zheng, S.Z. Qiao, R. Xu, Energy Environ. Sci. 9 (2016) 2563–2570.
[30] Y.N. Chen, Y.B. Guo, H.J. Cui, Z.J. Xie, X. Zhang, J.P. Wei, Z. Zhou, J. Mater. Chem. A 6 (2018) 9716–9722.
[31] X.J. Cui, P.J. Ren, D.H. Deng, J. Deng, X.H. Bao, Energy Environ. Sci. 9 (2016) 123–129.
[32] Y.N. Chen, X. Zhang, H.J. Cui, X. Zhang, Z.J. Xie, X.G. Wang, Energy Storage Mater. 15 (2018) 226–233.
[33] S.H. Ahn, A. Manthiram, Small 13 (2017) 1702068.
[34] S. Dresp, F. Luo, R. Schmack, S. Kühl, M. Gliech, P. Strasser, Energy Environ. Sci. 9 (2016) 2020–2024.
[35] G.T. Fu, Z.M. Cui, Y.F. Chen, Y.T. Li, Y.W. Tang, J.B. Goodenough, Adv. Energy Mater. 7 (2016) 1601172.
[36] S. Li, C. Cheng, X.J. Zhao, J. Schmidt, A. Thomas, Angew. Chem. Int. Ed. 57 (2018) 1856–1862.
[37] B. Wang, C. Tang, H.F. Wang, B.Q. Li, X.Y. Cui, Q. Zhang, Small Methods 2 (2018) 1800055.
[38] S. Singh, D. Kumar, V. Dhavale, D. Pal, S. Kurungot, Adv. Mater. Interfaces 3 (2016) 1600532.
[39] Y.J. Huo, X.Y. Peng, X.J. Liu, J. Luo, ACS Appl. Mater. Inter. 10 (2018) 12618–12625.
[40] H.Y Li, L.H. Zhang, L. Li, C.W. Wu, Y.J. Huo, Y. Chen, X.J. Liu, X.X. Ke, J. Luo, G.V. Tendeloo, Nano Res. doi.org/10.1007/s12274-018-2172-z.
[41] W.X. Yang, X.J. Liu, X.Y. Yue, J.B. Jia, S.J. Guo, J. Am. Chem. Soc. 137 (2015) 1436–1439.
[42] A. Mukhtar, B.S. Khan, T. Mehmood, Appl. Phys. A 122 (2016) 1022.
[43] H.Y. Lu, D.B. Sun, H.Y. Yu, J. Alloy Compd. 546 (2013) 229–233.
[44] Y. Hou, S.M. Cui, Z.H. Wen, X.R. Guo, X.L. Feng, J.H. Chen, Small 11 (2015) 5940–5948.
[45] X.H. Tang, H.Y. Ng, Electrochim. Acta 247 (2017) 193–199.
[46] J. Zhang, C.Y. Zhang, Y.F. Zhao, I.S. Amiinu, H. Zhou, X.B. Liu, Y.F. Tang, S.C. Mu, Appl. Catal. B-Environ. 211 (2017) 148–156.
[47] L. Xu, Q.Q. Jiang, Z.H. Xiao, X.Y. Li, J. Huo, S.Y. Wang, L.M. Dai, Angew. Chem. 128 (2016) 5363–5367.
[48] X.Z. Yue, S.S. Yi, R.W. Wang, Z.T. Zhang, S.L. Qiu, Appl. Catal. B-Environ. 224 (2018) 17–26.
[49] Y. Shen, Y.F. Zhou, D. Wang, X. Wu, J. Li, J.Y. Xi, Adv. Energy Mater. 8 (2018) 1701759.
[50] H.Y. Li, W.J. Wan, X.J. Liu, S.B. Shen, F. Lv, J. Luo, ChemElectroChem 5 (2018) 1113–1119.
[51] S. Dou, L. Tao, J. Huo, S.Y. Wang, L.M. Dai, Energy Environ. Sci. 9 (2016) 1320–1326.

[52] J. Ying, J. Li, G.P. Jiang, Z.P. Cano, Z. Ma, C. Zhong, D. Su, Z.W. Chen, Appl. Catal. B-Environ. 225 (2018) 496–503.

[53] Y.B. Li, C. Zhong, J. Liu, X.Q. Zeng, S.X. Qu, X.P. Han, Y.D. Deng, W.B. Hu, J. Lu, Adv. Mater. 30 (2018) 1703657.

[54] L.H. Zhang, L.L. Han, H.X. Liu, X.J. Liu, J. Luo, Angew. Chem. Int. Ed. 56 (2017) 13694–13698.

[55] X.J. Liu, W. Xi, C. Li, X.B. Li, J. Shi, Y.L. Shen, J. He, L.H. Zhang, L. Xie, X.M. Sun, P. Wang, J. Luo, L.M. Liu, Y. Ding, Nano Energy 44 (2018) 371–377.

[56] Z.X. Pei, H.F. Li, Y. Huang, Q. Xue, Y. Huang, M.S. Zhu, Z.F. Wang, C.Y. Zhi, Energy Environ. Sci. 10 (2017) 742–749.

[57] H.B. Yang, J.W. Miao, S.F. Hung, J.Z. Chen, H.B. Tao, X.Z. Wang, L.P. Zhang, R. Chen, J.J. Gao, H.M. Chen, L.M. Dai, B. Liu, Sci. Adv. 2 (2016) e1501122.

[58] A. Pendashteh, J. Palma, M. Anderson, R. Marcilla, Appl. Catal. B-Environ. 201 (2017) 241–252.

[59] C. Tang, B. Wang, H.F. Wang, Q. Zhang, Adv. Mater. 29 (2017) 1703185.